International Journal of Applied Earth Observation and Geoinformation 127 (2024) 103679

Contents lists available at ScienceDirect

International Journal of Applied Earth Observation and Geoinformation

journal homepage: www.elsevier.com/locate/jag

# Detection of oak decline using radiative transfer modelling and machine learning from multispectral and thermal RPAS imagery

A. Hornero [a,b,*], P.J. Zarco-Tejada [b,a], I. Marengo [c], N. Faria [c], R. Hernández-Clemente [d,e]

[a] Instituto de Agricultura Sostenible (IAS), Consejo Superior de Investigaciones Científicas (CSIC), Avenida Menéndez Pidal s/n, 14004 Córdoba, Spain
[b] School of Agriculture, Food and Ecosystem Sciences (SAFES), Faculty of Science (FoS), and Faculty of Engineering and Information Technology (FEIT), University of Melbourne, Melbourne, Victoria, Australia
[c] Department of Monitoring and Diagnosis, InnovPlantProtect Associação, 7350-999 Elvas, Portugal
[d] Departamento de Ingeniería Forestal, Universidad de Córdoba, Campus de Rabanales, Crta, IV, km. 396, E-14071 Córdoba, Spain
[e] Department of Geography, Swansea University, SA2 8PP Swansea, United Kingdom

A R T I C L E I N F O

*Keywords:*
Multispectral
Thermal
Radiative transfer
Disease detection
Artificial intelligence
RPAS
Machine learning
Forest health

A B S T R A C T

Oak trees are declining at an unprecedented rate due to the interaction of many factors, such as pests, diseases, droughts, pollution and flooding. Such abiotic- and biotic-induced stress produces anomalies in plant physiological and functional traits (PTs) that may be spectrally detected, serving to quantify trees' health status and condition. Previous studies have demonstrated that PTs' dynamic response can be tracked with hyperspectral and thermal images acquired via aerial platforms. However, the ability to detect the decline at different stages of severity among distinct oak species by using high-resolution multispectral images acquired via miniaturised cameras located aboard unpiloted airborne platforms is still unknown. This cost-effective approach offers improved operability to perform missions with greater continuity and replicability, which is critical to assess the decline progression. In this work, we evaluated the use of airborne multispectral and thermal imagery coupled with a 3-D radiative transfer modelling and machine learning approach for detecting *Phytophthora*-infected holm oak and cork oak trees. The field study included 2299 trees classified into disease severity classes with a gradient in levels of disease incidence located in Portugal (Ourique and Avis) and Spain (Huelva and Alcuéscar). The classification model achieved an overall accuracy of 76 % ($kappa = 0.51$) in detecting decline for both species, successfully identifying up to 34 % of declining trees that were not initially detected by visual inspection and confirmed in a reevaluation six months later. When compared against airborne hyperspectral imagery, results yielded comparable accuracy, with a relative decrease of ca. 4 % in overall accuracy and an average Cohen's kappa decrease of 7 %. The results further showed that classification using only hyperspectral imagery is slightly lower but equivalent to using combined multispectral and thermal data, and those derived from these sensors independently are not adequate to classify the different severity stages. The proposed model has enabled us to effectively discern various stages of decline in cork and holm oak forests across diverse geographical areas. Our study, therefore, demonstrates that the tandem use of multispectral and thermal sensors onboard a remotely piloted aircraft platform, together with a radiative transfer modelling and machine learning approach, helps us to predict the impact of this particularly damaging disease on oak trees. This capability facilitates the detection and swift mapping of disease progression, ensuring a proactive approach to forest management.

## 1. Introduction

Oak decline has been severely affecting the distribution of *Quercus suber* (cork oak) and *Quercus ilex* (holm oak) across the Mediterranean basin since 1980 (Camilo-Alves et al., 2013). It is challenging to identify the factors triggering oak decline produced by complex stressors interaction such as abiotic (water stress, loss of nutrients and soil compaction) and biotic stresses (pests, parasites and pathogens) (Camilo-Alves et al., 2017). The interactions are mainly attributed to the combination of water stress increasing the weakening of the trees and the attack of different pathogens, in particular, root rot caused by pathogens (*Phytophthora cinnamomi* and *Pythium spiculum*) (Colangelo

* Corresponding author.
*E-mail address:* alberto.hornero@csic.es (A. Hornero).

https://doi.org/10.1016/j.jag.2024.103679
Received 4 December 2023; Received in revised form 11 January 2024; Accepted 22 January 2024
1569-8432/© 2024 The Authors. Published by Elsevier B.V. This is an open access article under the CC BY license (http://creativecommons.org/licenses/by/4.0/).

et al., 2018). In this scenario, the necessity for real-time or predictive precision mapping becomes evident, as it plays a pivotal role in effectively managing the spatial spread of the pest and expediting the restoration of the ecosystem.

Nonetheless, the constrained availability of in-situ forest health datasets hinders the comprehensive analysis of large-scale forest decline processes. Yet, combined with remote sensing data, these datasets present a valuable opportunity to create mapping products for identifying and analysing these processes across diverse spatial scales (Pause et al., 2016). Most studies were initiated by combining field data observations of visual defoliation with a spectral imaging transformation of two or more red and infrared bands (Castellaneta et al., 2022; Hernández-Lambraño et al., 2019). The main limitation of this approach in forest canopies is that, in most cases, once damage becomes visible, tree recovery is often irreversible (Hernández-Clemente et al., 2019; Varner et al., 2021).

In their efforts to address this challenge, Hernández-Clemente et al. (2017) evaluated hyperspectral and thermal data of oak decline through the analysis of different plant functional traits (PTs) showing physiological anomalies corresponding to the physiological decline. Soil-dwelling root pathogens like *Phytophthora* or *Pythium* can cause severe functional damage to oak trees, affecting transpiration and key plant characteristics (Contreras-Cornejo et al., 2023). These pathogens disrupt the tree's vascular system, leading to reduced transpiration, impaired photosynthesis, and chlorosis. These effects often resemble symptoms of water stress, making it challenging to achieve accurate diagnosis unless we employ the quantification of alterations in plant traits. Similar approaches have been successfully proposed and validated in species such as olive and almond trees, where the combined use of inverted PTs from hyperspectral and thermal images has been used to detect *Xylella fastidiosa* disease with overall accuracies exceeding 92 % (Zarco-Tejada et al., 2021). Furthermore, the inversion of PTs through radiative transfer models helps to understand the physiological alteration of affected trees, which is critical for assessing the health condition of the trees (Zarco-Tejada et al., 2018). In the case of holm oak trees, the inversion of PTs from hyperspectral images and thermal data has been successfully used to predict oak decline up to two years in advance (Hornero et al., 2021b). However, the replicability of these approaches is linked to the need for high-resolution hyperspectral and thermal data acquired with airborne platforms that offer sufficient stability to collect high-quality data. Unfortunately, the logistics and cost required for airborne campaigns constrain the continuous assessment of forest canopies, which is essential for assessing the temporal and spatial changes of the holm oak decline processes (Liu et al., 2007).

Alternatively, using remotely piloted aircraft systems (RPASs) could increase the spatial resolution, minimise the response time and reduce the time required for interpreting PTs. RPASs provide high-resolution imagery and real-time data with sensor customisation flexibility. The capability to deal with large areas with RPAS imagery is limited, but it can be used to complement satellite data in detail on areas of interest. Moreover, RPASs offer the versatility of acquiring imagery in poorly accessible areas, adapting and modifying sensors quickly, and enabling continuous data collection (Fraser and Congalton, 2021). This aspect is essential for analysing physiological changes, which serve as early indicators of health conditions in the case of declining holm oak (Hernández-Clemente et al., 2017). However, despite all the versatility offered by RPASs, they also have significant limitations that have constrained their use in forest disease detection (Ecke et al., 2022), such as i) the stability of the aircraft, RPAS vibrations can affect the spectral quality of the images, which is a critical issue when narrow bands of hyperspectral sensors are used (Honkavaara et al., 2017; Oliveira et al., 2019); ii) the weight of the payload can limit the number and size of sensors used, which is quite limiting when the study requires the use of hyperspectral and thermal cameras; iii) the flight extension due to the limited endurance of the platforms; iv) in the case of thermal sensors, uncooled thermal systems affect the temperature of the images under ambient flight conditions (Maes et al., 2017; Olbrycht and Więcek, 2015), thus thermal drift must be corrected continuously; and v) typical multispectral cameras used with RPASs cannot measure essential traits such as the normalised phaeophytinization index (NPQI) and the normalised photochemical reflectance index (PRIn) xanthophyll proxy, result in poorer vascular disease detection (Poblete et al., 2023); their broad bandwidth fails to capture subtle physiological changes indicated by narrow-band features such as chlorophyll fluorescence and xanthophyll variations.

Despite these limitations, there is a diverse selection of affordable sensors capable of collecting data across the visible, infrared, and thermal spectrums. These sensors may serve as valuable tools for monitoring plant growth, structure, and functionality (Tian et al., 2017). Notably, in assessing functionality, research has shown that the temperature difference between the tree crown and the surrounding air, as measured by airborne sensors, is one of the most effective early indicators of *Phytophthora* infection in oak trees (Hernández-Clemente et al., 2017; Hornero et al., 2021b). Thus, this variable could help to increase the detection capability of low-cost RPAS merely based on multispectral sensors. However, the assessment of the suitability of RPAS-based sensors in detecting oak decline is still unknown. Hence, this study aims to assess the effectiveness of an RPAS-based system equipped with an affordable image acquisition setup comprising multispectral and thermal sensors. It aims to employ machine learning (ML) techniques for the detection of forest decline processes in oak forests, comparing the results with high-resolution hyperspectral and thermal imagery, which serve as a benchmark.

## 2. Materials and methods

### 2.1. Study site and field survey

The study was conducted in open oak forests (i.e., Mediterranean-like oak savannah known as *Montado* in Portugal and *Dehesa* in Spain) located in Puebla de Guzmán (Andalucía, Huelva; southwestern Spain, 37°36′30.89″N, Lon 7°20′27.97″W), Alcuéscar (Extremadura; central Spain, 39°9′39.42″N, O6°13′27.95″W), Ourique (District of Beja; southern Portugal, 37°37′12.2″N 8°13′54.3″W) and Avis (District of Portalegre; central Portugal, 39°5′12″N, 7°54′10″W). The vegetation in the study areas was mainly dominated by oak-dispersed trees (*Quercus ilex* and *Quercus suber* species). During the sampling, we use the disease severity (DS) and disease incidence (DI) classification defined by Seem (1984), describing DS as the quantity of disease-affecting entities within a sampling unit and DI as a quantitative measure, defined as the proportion of diseased entities within a sampling unit. Based on visual inspection, we assigned individual trees to one of the four available DS categories (Fig. 1), determined by the percentage of crown defoliation and other *Pc*-related symptoms (Eichhorn et al., 2016), with each individual serving as a sampling unit. For a more accurate assessment of DS, we considered not only the defoliation of the crown but also other typical Pc-induced symptoms, such as the presence of stem cankers and the emergence of adventitious epicormic sprouts, following the guidelines of Jung et al. (2000). Furthermore, to avoid ambiguities, we specify the part of the crown including all living branches and thin branches that are dead but still retain leaves. We excluded thick branches that have been dead for years and have already lost their natural buds, epicormic shoots below the crown, and gaps where branches have never existed. This methodological precision follows the classification of the Andalusian Forest Damage Monitoring Network (Consejería de Medio Ambiente y Ordenación del Territorio, 2018).

Based on the visual inspection DS ranged from zero, indicating the absence of visual symptoms, to three, when most of the branches in the crown were dead (Fig. 1). DI was either affected or unaffected (one or zero on a binary scale), where non-symptomatic trees corresponded to a DS of zero and symptomatic trees to any other severity level (DS higher than zero).

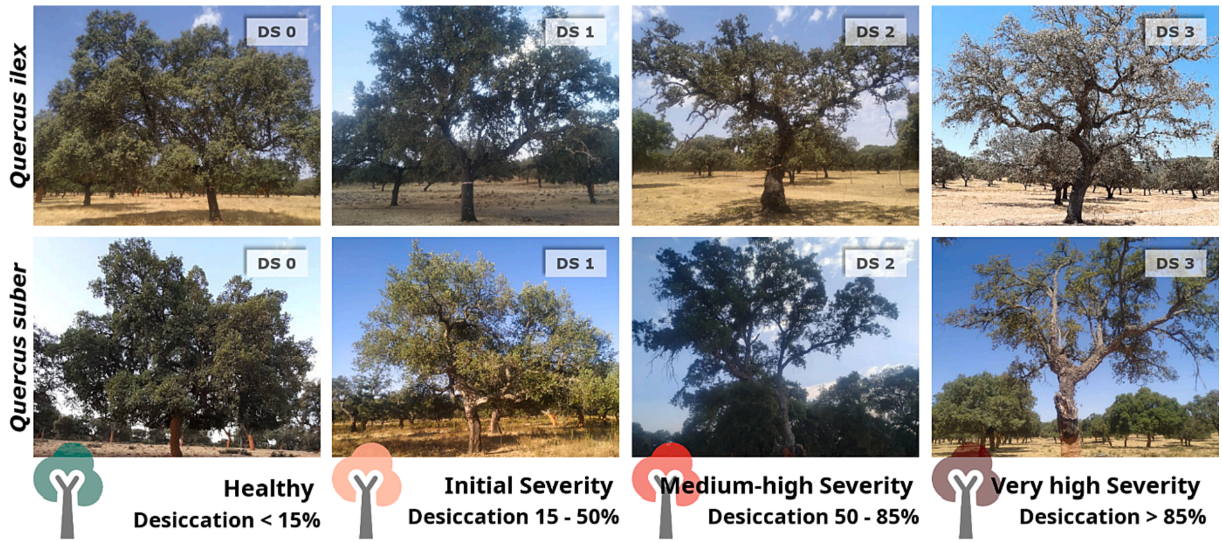


**Fig. 1.** Examples of the four forest disease severity (DS) levels assigned to *Quercus suber* and *Quercus ilex* during the field survey. DS ranged from 0, indicating symptomless, to 3, with very high to extreme severity. Initial severity, showing few desiccated branches affecting a limited part of the canopy; Medium-high severity, indicating desiccation of a large part of the canopy; Very high severity, describing a canopy with evenly distributed desiccated branches.

**Table 1**
Field surveys (FS) and aerial campaigns (AC) carried out to conduct the data collection.

| Location | 2017 | 2021 | 2022 | Aerial Campaign |
|---|---|---|---|---|
| Huelva (ES) | FS + AC | | | Aircraft with hyperspectral and thermal |
| Alcuéscar (ES) | | FS + AC | FS | RPAS with multispectral and thermal |
| Ourique (PT) | | FS + AC | FS | RPAS with multispectral and thermal |
| Avis (PT) | | FS + AC | FS | RPAS with multispectral and thermal |

In the field survey carried out in the summer of 2017, we assessed a total of N = 1146 trees in Puebla de Guzmán, including the DS and DI for individual holm oak trees (100 %). In the sampling conducted in the summer of 2021, we assessed 367 trees in Avis, 391 trees in Ourique and 395 trees in Alcuéscar, including the DS and DI for individual holm (33.5 %) and cork oak trees (66.5 %) (N = 1153) (Table 1). The field surveys were repeated in the summer of 2022 to analyse the prediction capability of the models through false-positive observation rates.

### 2.2. *High-resolution imagery*

#### 2.2.1. *Piloted aircraft campaigns*

High-resolution hyperspectral images were collected onboard a Cessna 172 aircraft operated by the Laboratory for Research Methods in Quantitative Remote Sensing (QuantaLab) on the 19th of July 2017 in Puebla de Guzmán, Huelva. The imaging equipment included a visible near-infrared hyperspectral imager and a thermal camera (Fig. 2). The aircraft flew at 350 m above ground level, covering a ground surface area of 720 ha in a cloudless sky. The visible near-infrared (VIS-NIR) camera (Hyperspec VIS-NIR, Headwall Photonics Inc., MA, USA) collected 260 spectral bands and a ground resolution of 60 cm, allowing for the identification of individual oak tree crowns. Additional technical details can be found in Zarco-Tejada et al. (2013). The thermal sensor used in the study was the FLIR SC655 (Teledyne FLIR LLC, OR, USA) with a resolution of 640 × 480 pixels. It had a 24.5-mm lens with an angular field of view (FOV) of 45 × 33.7°, resulting in a ground resolution of 60 cm/px. The sensor had an uncooled microbolometer focal plane array and operated within a spectral range of 7.5 to 14 µm. It included a thermoelectric cooling (TE) stabilisation system, providing a thermal sensitivity below 50 mK.

The methodology employed in the study involved the radiometric calibration of the hyperspectral sensor using an integrating sphere (STM-USS-2000C, Labsphere Inc., NH, USA) at four characterised illumination levels. Atmospheric correction for the VIS-NIR sensor was achieved using a field spectroradiometer coupled with a cosine corrector (ASD HandHeld Pro, Malvern Panalytical Ltd., United Kingdom). Cross-track correction was applied to account for illumination and viewing angle effects. Thermal calibration was conducted in the laboratory using a black body calibration source (LANDCAL P80P, Land Instruments International Ltd., United Kingdom) and ground temperature measurements described by Calderón et al. (2015). Tc-Ta was determined by subtracting weather station air temperature from calibrated thermal imagery. Orthorectification of hyperspectral and thermal images was performed using PARGE (ReSe Applications GmbH, Switzerland) and Pix4DMapper (Pix4D SA, Switzerland) software, respectively, following established pre-processing and correction procedures outlined in previous studies by Hernández-Clemente et al. (2012) and Zarco-Tejada et al. (2013).

#### 2.2.2. *RPAS campaigns*

We collected very high-resolution images in the three locations between the 20th and 22nd of September 2021 using a multi-lens multispectral camera (MicaSense RedEdge-M, AgEagle Sensor Systems Inc., KS, USA) and a thermal camera – FLIR Tau 2 640 (FLIR Systems, Wilsonville, OR, USA) – installed in tandem onboard a Skymapper SKM2 VTOL platform, a Foxtech Loong 2160′s customised version (Fig. 3, Table 2). The flights were conducted over three locations in Portugal (Avis and Ourique) and Spain (Alcuéscar) (Fig. 3) in clear sky conditions. The imagery was acquired at 120 m AGL with the RPAS flying on the solar plane and a surveyed area of 145 ha. The five sensors of the multispectral device covered the visible and near-infrared region (475–20, 560–20, 668–10, 717–10 and 840–40 nm) with a ground resolution of 7.5 cm/px; surface reflectance was derived through atmospheric correction pointing to a calibrated reflectance panel before takeoff and just after landing. In addition, the single-channel (7.5 – 13.5 µm) miniaturised infrared thermal sensor (13 mm lens) produced images at

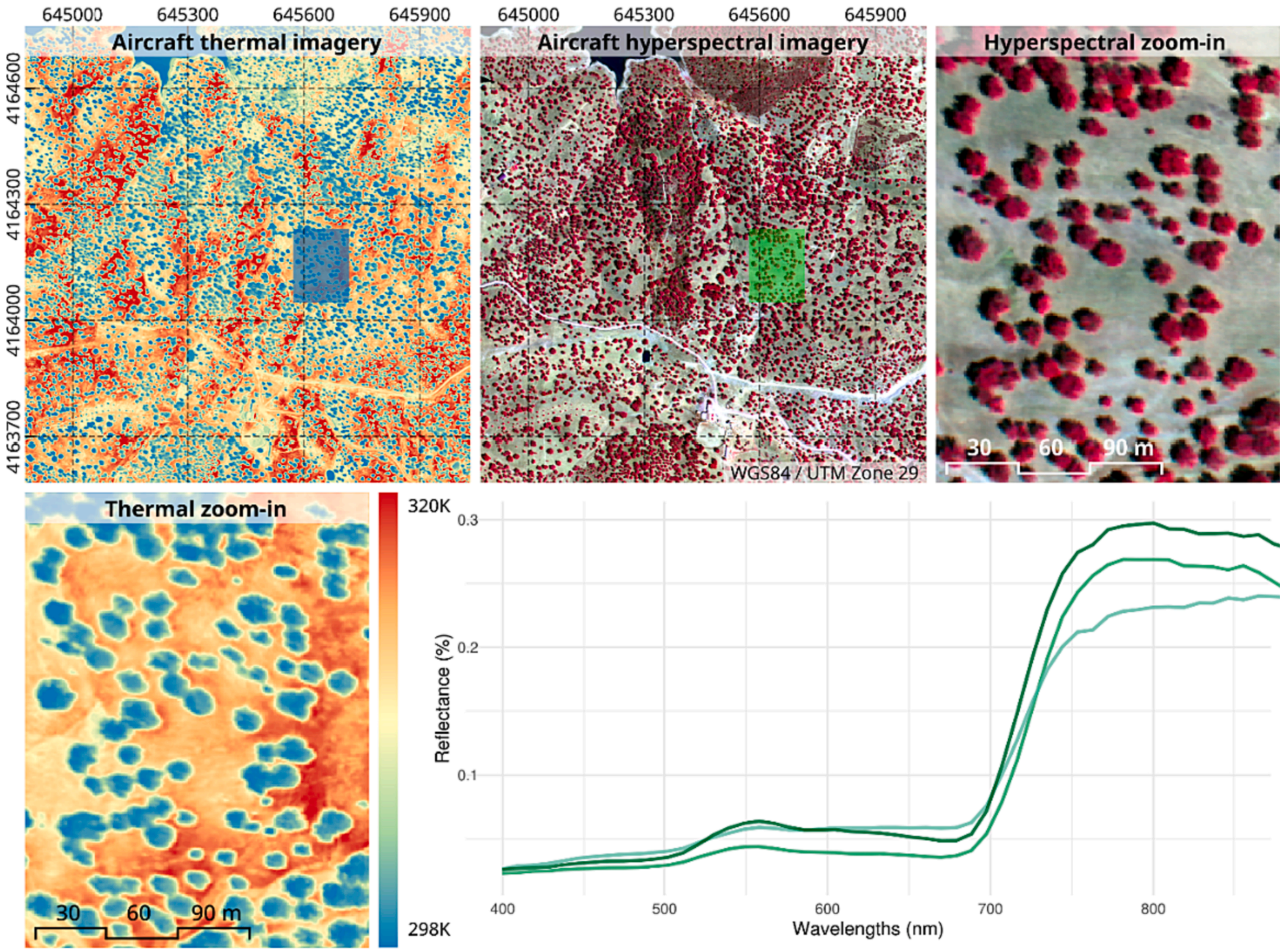


**Fig. 2.** Airborne remote sensing composite displaying high-resolution hyperspectral and thermal imagery over the study area in Huelva (Spain). On the left, the thermal imagery with the colour scale indicates variations in heat across the landscape, further detailed in the lower zoom-in panel. On the top right, the hyperspectral sensor acquires detailed reflectance data across a broad spectrum of wavelengths, enabling precise identification and analysis of individual trees. The graph below shows spectral signatures of three distinct measurements of vegetation above the canopy.

16 cm/px, and was calibrated using ground temperature measurements from two fabrics and bare soil with a handheld thermometer (LaserSight LS LT, Optris GmbH, Berlin, Germany). Multispectral and thermal mosaics and zoomed-in overviews for each location are shown in Fig. 4.

The process of generating the orthomosaic was carried out using Pix4D photogrammetry software. Image correction and data preprocessing are described in detail in Hernández-Clemente et al. (2012). The high-resolution imagery acquired from each camera allowed us to identify and delineate tree crowns independently. This image processing was achieved by using object-based segmentation methods through the Mahalanobis multivariate direction-sensitive distance classifier (Richards and Jia, 1999), and a binary watershed analysis using the Euclidean distance map to automate the separation of trees with overlapping crowns (Fig. 4), seeking to minimise the effect of background and shadowing. Vegetation indices (VIs) – 36 in total – were selected from Hornero et al., (2021b), choosing those centred or close to the band centres used in each index, regardless of their spectral width (Appendix A).

### 2.3. Analytical framework

The image data from both airborne and RPAS were used to quantify the PTs using RTM, as detailed in section 2.4, and to develop the predictive forest health models following the methods outlined in section 2.5.

Before conducting the RPAS flights, an analysis was performed to assess the impact of bandset reduction on the detection of forest decline. To achieve this, a reanalysis was carried out on the airborne hyperspectral and thermal data in conjunction with a field survey conducted during the summer of 2017 to assess oak decline in Huelva, Spain. This reanalysis involved the creation of a spectrally resampled multispectral image product derived from airborne hyperspectral imagery, hereafter referred to as the “HBR product” – which stands for RPAS-based hyperspectral band set reduction (HBR). This product mimicked the spectral bands offered by the Micasense RedEdge-M (Fig. 5). Subsequently, the HBR product was employed to develop a classification model for the detection of oak decline, utilising the same field assessment dataset (N = 1146) as employed by Hornero et al., (2021b). The accuracy of the HBR product was then compared with the results obtained from the original aircraft-based sensors (hyperspectral and thermal).

Following the evaluation of the RPAS-based HBR product, the same setting was applied to the image data collected during the RPAS campaign to analyse the contribution of PTs in detecting forest health and to create a forest health classification model for the study sites in Avis, Ourique, and Alcuescar, employing the same methodology.

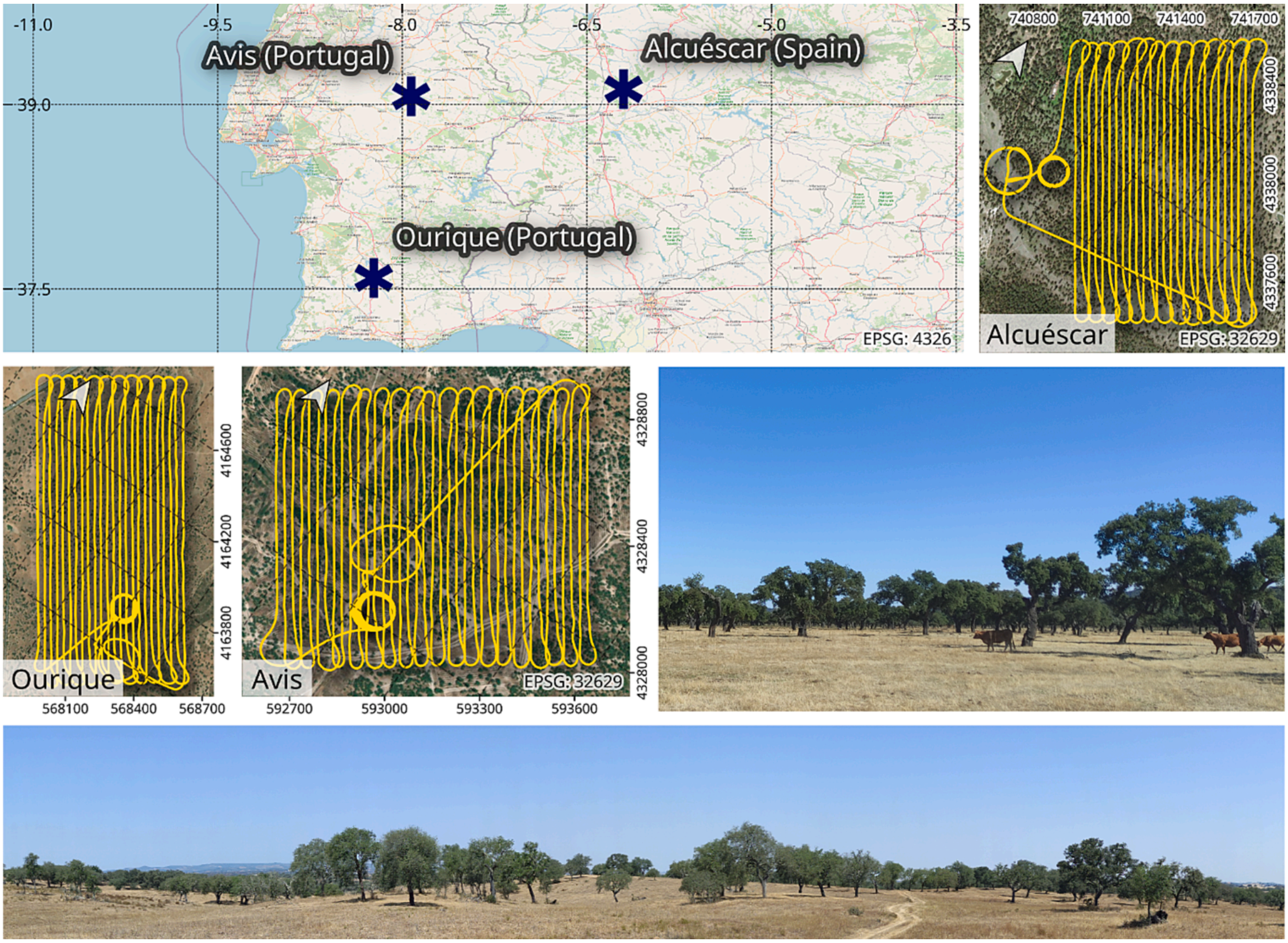


**Fig. 3.** RPAS-based data acquisition conducted over three areas in Portugal (Avis and Ourique) and Spain (Alcuéscar). The yellow lines represent the flight plan. On the middle right and bottom, pictures show the heterogeneity of the landscape within the areas of study. (For interpretation of the references to colour in this figure legend, the reader is referred to the web version of this article.)

**Table 2**
Technical characteristics of the airborne and RPAS sensors and operational settings.

| | Multispectral Camera | Thermal Camera |
|---|---|---|
| Sensor model | Micasense RedEdge-M | FLIR Tau 2 |
| Spectral range (nm) | 475 ± 20; 560 ± 20; 668 ± 10; 717 ± 10; 840 ± 40 | 7500 – 13,500 |
| Resolution (px) | 5 x 1280 x 960 | 640 x 480 |
| Focal length (mm) | 6 | 13 |
| Storage | SD card | microSD card |
| Communication | WiFi | AV output + buttons |
| Capture mode | Triggered (location-based from autopilot) | Continuous |
| Geopositioning | Absolute position via GPS | Time-synchronised |

### *2.4. Retrieval of plant functional traits from canopy reflectance and radiative transfer models*

The quantification of the biochemical components and structural parameters was performed through an inversion of a 3-D radiative transfer model (RTM) for the pixels extracted from the tree crowns (Fig. 6). Using prior information from the environment of possible parameters, the ill-posed problem of the model inversion could be substantially mitigated. First, the input variables to the model were established according to the existing literature, and nominal parameters (Hernández-Clemente et al., 2017; Hornero et al., 2021b), to ensure that the generated look-up table (LUT) covered the range of spectral variability of the tree crowns (Appendix B). Then, we built a LUT of more than 1 M simulations using the PROSPECT-D leaf model (Feret et al., 2017) coupled with the FLIGHT8 canopy model (Hornero et al., 2021a; North, 1996). In the first stage, we determined the leaf area index (LAI), the chlorophyll ($C_{ab}$) and the carotenoid ($C_{ca}$) content, setting to nominal values of anthocyanin ($A_{nth}$), water and dry matter ($C_{dm}$) content, and the structural parameter N to a value previously determined (Hernández-Clemente et al., 2017). The LUT-based inversion scheme was a multi-step approach where the LAI values were initially retrieved, and then $C_{ab}$ and $C_{ca}$, using the MSR, PSSRb and CRI700 VIs as proxies for each PT, respectively. In the subsequent phase, the parameterisation retrieved for each tree was used to specifically quantify $A_{nth}$ and $C_{dm}$, using mARI and spectral fitting, respectively.

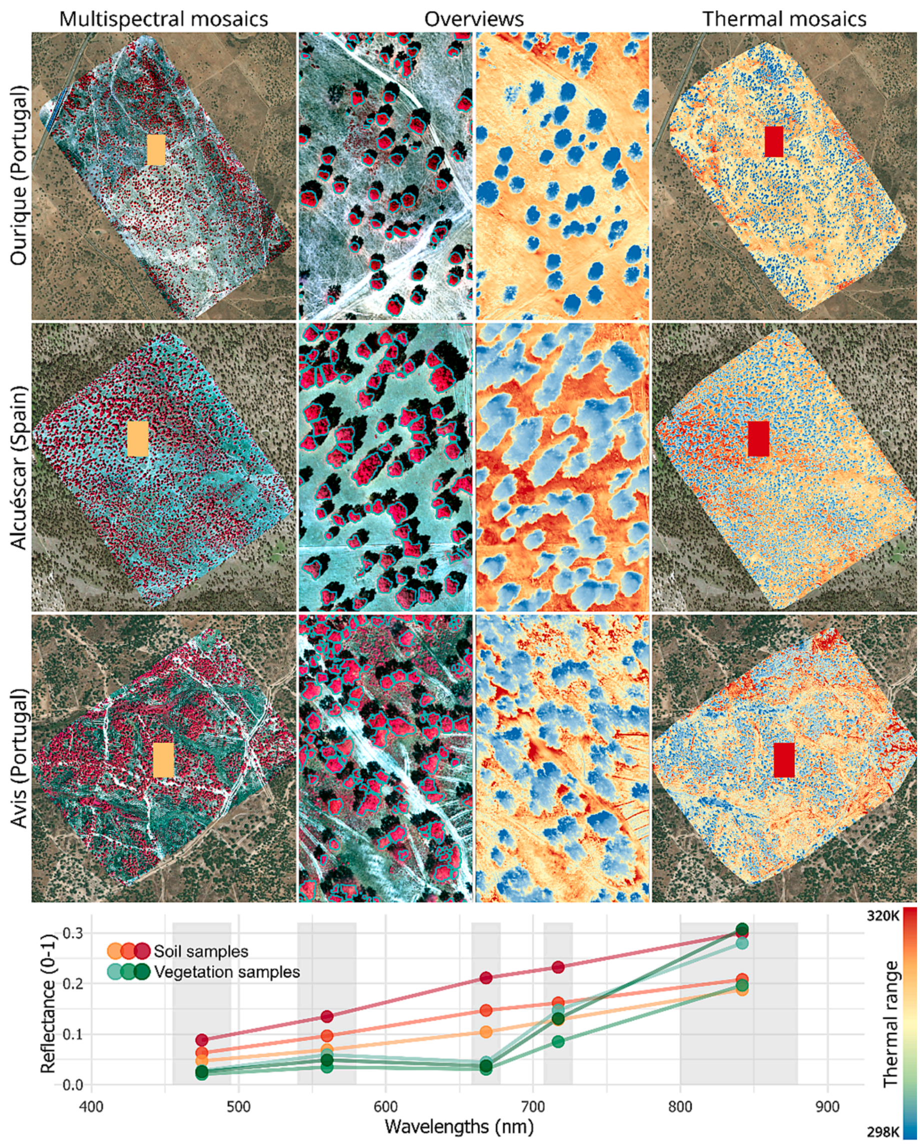


**Fig. 4.** RPAS-based very high-resolution multispectral and thermal imagery acquired over the three surveyed areas located in Portugal (Avis and Ourique) and Spain (Alcuéscar). Depicted on each side is a zoomed-in overview. The outlined segmentation for each tree is shown over the multispectral overviews coloured in vibrant cyan. The graph below illustrates the spectral reflectance of various vegetation and soil samples, highlighting the percentage of light they reflect in a range of wavelengths within the multispectral configuration from the visible to the near-infrared spectrum. (For interpretation of the references to colour in this figure legend, the reader is referred to the web version of this article.)

### 2.5. *Predictive classification model assessment*

The workflow for assessing the predictive models involved two main steps: i) a feature selection analysis to evaluate the contribution and significance of each variable to generate the classification model, and ii) a subsequent evaluation of model performance, including assessing various classification methods and accuracy measures (Fig. 7).

The feature selection uses as input data the field survey of affected and non-affected tree locations and the VIs and PTs retrieved from the images (Fig. 7**a**). The analysis was performed through a random decision forest classification (DFC) (Breiman, 2001) to identify the importance of the variables (PTs and VIs independently) using an adaptation of Kursa and Rudnicki, (2010). To determine the set of variables to be used in the classification model, an aggregation stage was established (with an order according to their importance). Then, the VIs were added based on their importance. Next, the variance inflation factor (VIF) was calculated in each iteration to avoid multicollinearity among the predictor variables, setting the threshold value at 10. If the VIF exceeded this threshold in any variable, the last variable added was discarded. Finally, a Pearson correlation analysis was established to determine the correlations between pairs by setting a cut-off filter of 0.85 (Dormann et al., 2013) to complete the selection of variables. As an additional step, the feature selection using the DFC process was used to assess the importance of each selected variable contributing to the model's predictive performance.

The accuracy assessment of the reliability of models for the detection of oak decline (Fig. 7**b**) was performed using data from different sites and species. Two ML algorithms were employed: a supervised non-linear support vector machine (SVM) with a Gaussian radial base kernel function (Scholkopf et al., 1997) and a random forest (RF) algorithm (Breiman, 2001). These algorithms have been recognised as primary classifiers in airborne imaging (Gigović et al., 2019; Liu et al., 2017). We employed class weights in ML, following the method described in He and Cheng (2021), to ensure that our results were comparable to those obtained from the datasets collected in Alcuescar, Avis, and Ourique, where a significant between-class imbalance was observed (DS0: 24.8 %;

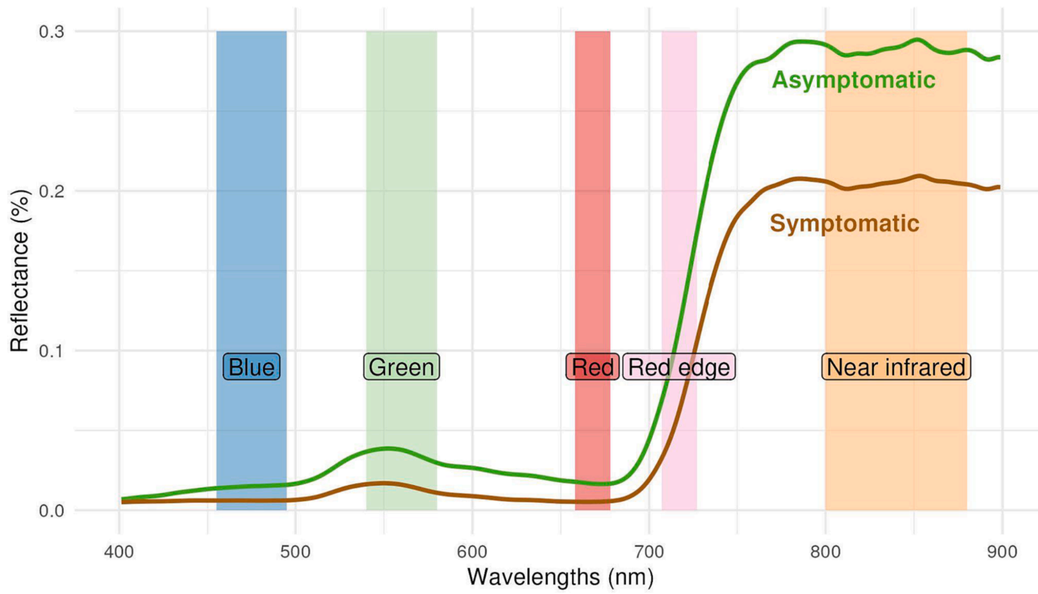


**Fig. 5.** Example of spectral data from symptomatic and asymptomatic oak trees from an RPAS-based band reduction product of a hyperspectral image and the full range of bands provided by the same sensor.

DS1: 36.4 %; DS2: 26.4 %: DS3: 12.4 %).

To validate these models, we conducted 100 iterations, randomly splitting the dataset into 80 % training and 20 % test samples, utilising k-fold cross-validation with ten equal-sized subsamples repeated five times. Subsampling training data in each iteration ensured balanced class frequencies. We evaluated classification accuracy using overall accuracy (OA) and Cohen's kappa coefficient (κ) to measure agreement beyond chance (Landis and Koch, 1977).

Finally, we investigated whether the models could anticipate trees assessed as asymptomatic in the first assessment and otherwise in the subsequent evaluation. This analysis helped to calibrate the model's ability to predict future estimates of forest decline based on image data and previous assessments.

## 3. Results

### 3.1. *Impact of a hyperspectral bandset reduction on the detection model accuracy*

The contribution of plant traits derived from the hyperspectral data simulating the RPAS-based HBR product was analysed for the detection of oak decline (Fig. 8). As previously documented (Hornero et al., 2021b; Poblete et al., 2023; Zarco-Tejada et al., 2021), it is worth noting that tree-crown (Tc) –normalised by ambient temperature (Ta) in the form Tc-Ta or via the Crop Water Stress Index (CWSI)– exerts a substantial global impact on both incidence and severity, while other plant traits like LAI, $C_{dm}$, $C_{ca}$, $C_{ab}$, and $A_{nth}$ make comparatively smaller contributions.

Increasing Tc-Ta values with rising severity levels are tied to a decrease in LAI (as seen in Fig. 9). The distribution of LAI values across different severity and incidence levels demonstrates a consistent pattern in both the original hyperspectral product and the RPAS-based HBR product. LAI decreases as severity and temperature increase, while it rises with damage levels. In both scenarios, there is a gradual reduction in LAI from levels 0 to 2 of severity, with the most significant drop occurring during the transition to level 3. This abrupt shift in LAI values from level 2 to level 3 corresponds to a similar sharp increase in Tc-Ta between these levels, as reduced vegetation structure amplifies the background effect.

The detection of oak decline combining the full range of bands of the hyperspectral imager and the thermal dataset using the RF classification model showed the highest accuracy with an OA of 81.2 % and a κ value of 0.62 for detecting DI levels, and an OA of 65.1 % and a κ value of 0.53 for detecting DS levels. These accuracies slightly decreased using the combined HBR and thermal dataset, showing an OA of 79.8 % and a κ value of 0.59 for detecting DI levels and an OA of 61.1 % and a κ value of 0.47 for detecting DS levels. Similar accuracies were observed in both cases using the SVM algorithm (Fig. 10, Table 3).

Comparatively, looking at the reliability of the individual sensors, the RF and SVM models computed using only the hyperspectral dataset yielded higher OAs than using HBR or the thermal dataset independently; the largest difference was found discriminating between incidence levels, with relative differences of 3 % and 7 % compared to the HBR and the thermal dataset, respectively (Table 3). It is noteworthy that the thermal sensor independently was not able to discriminate correctly between severity levels (κ below 0.4), showing a minimal level of agreement between predicted and observed values. The hyperspectral dataset results excel with better performance, at higher cost and complexity. The thermal sensor, with lower accuracy for severity classification, offers unique physiological insights when used independently, while the HBR dataset provides a practical balance of reliability and physiological interpretation.

Finally, it's important to highlight that the accuracy achieved with solely the hyperspectral dataset is marginally lower, averaging 2.3 % less, than using the HBR with thermal data, and 5 % below the combined hyperspectral and thermal dataset. However, when utilising an RPAS for data collection, integrating HBR with thermal data becomes essential, ensuring reliability exceeds a kappa value (κ) of 0.47 for severity level discrimination and reaches κ = 0.59 for incidence level detection.

### 3.2. *Contribution of RPAS-based PTs for detecting progressive stages of decline*

Building upon the fair outcome obtained through the reduction of hyperspectral bands in the previous section, we delved deeper into assessing the contribution of PTs derived from multispectral RPAS imagery across three sites with oak decline located in Avis, Ourique, and Alcuescar. In Fig. 11, we show each PT along with their respective importance scores in distinguishing the severity and incidence of oak decline. The overall significance of these PTs underscores the substantial influence of Tc-Ta and LAI. Specifically, Tc-Ta emerges as the foremost contributor in distinguishing different levels of decline incidence (DI),

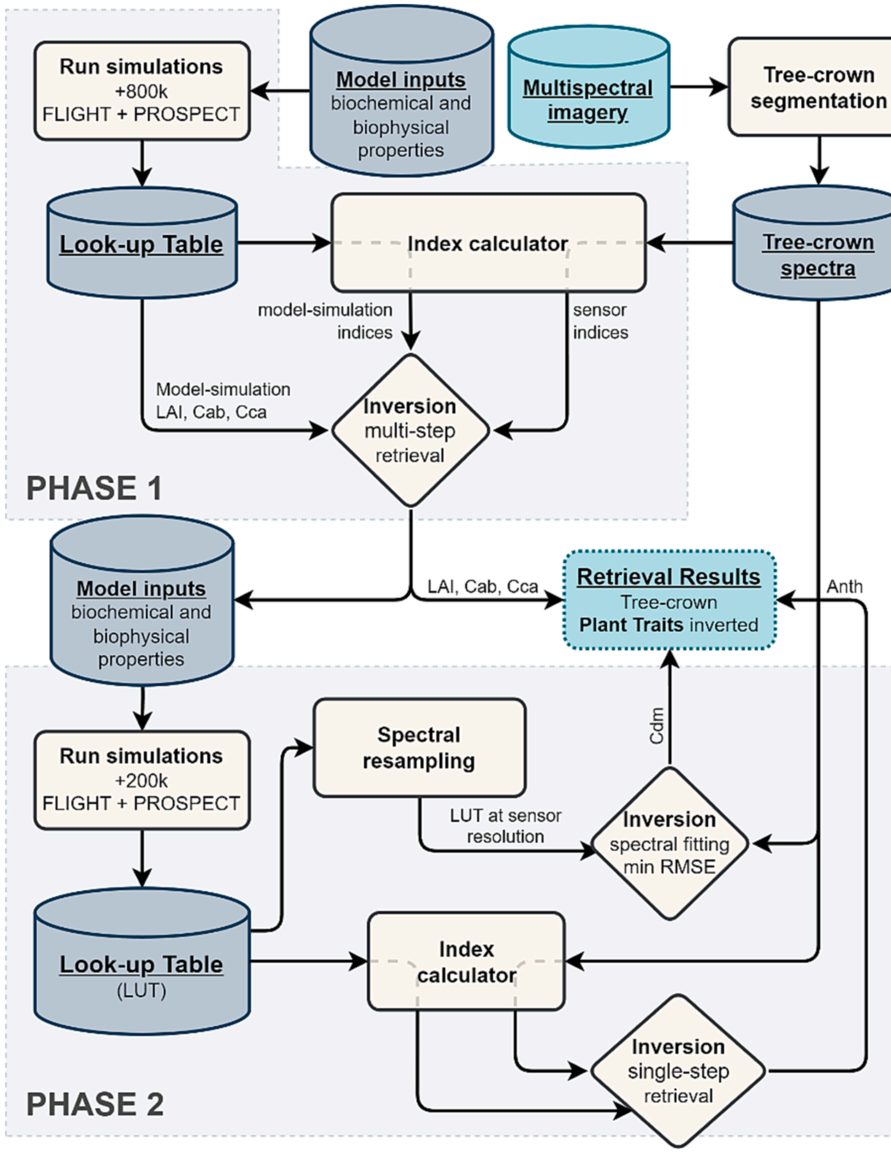


**Fig. 6.** Model simulation and analytical approach diagram.

while LAI prevails as the most critical variable for discerning decline severity (DS). In both cases, these two PTs are closely followed by others, including $C_{ca}$, $C_{dm}$, $C_{ab}$, and $A_{nth}$.

The change in PTs as the severity of the condition increases shows a consistent pattern, as depicted in Fig. 12. We observe a steady rise in Tc-Ta values as the severity levels increase, indicative of declining oak vitality and photosynthetic efficiency. This is accompanied by a decrease in LAI, reflecting reduced leaf area and health, and a reduction in the content of pigments (such as $C_{ca}$, $C_{dm}$, $C_{ab}$, and $A_{nth}$). As these variables decrease, we also observe an increase in the quantity of $C_{dm}$, which is linked to the loss of functionality or the accumulation of senescent material, a clear marker of advanced decline stages. This trend becomes more pronounced with higher severity levels.

We enhanced the analysis of PTs by including a set of indices. We carefully selected these indices through a rigorous screening process, ensuring that they had a VIF below 10. As a result, we employed DNCabxc, PSRI, and PRI to distinguish between DI levels, and PRIn and RCRI550 for assessing DS. This selection process followed the methodology outlined in Fig. 7**a** and was included as an input for computing the classification models to detect oak decline.

### 3.3. RPAS-based detection models of holm- and cork-oak decline

The accuracy of the models for DI and DS discrimination was computed through random forest and support vector machine as shown in Fig. 13. DI classification shows significantly better results than DS, a reasonable output considering the simplicity and straightforward discriminatory capacity of DI, which has an OA above 75 % and a κ above 0.5, considered fair to good estimates according to Fleiss et al. (2003). The accuracy retrieved by both models for the discrimination of DI and DS was higher in *Q. ilex* than in *Q. suber*, with maximum values of OA = 81.7 %, κ = 0.62 for *Q. ilex*, and OA = 74.9 %, κ = 0.49 for *Q. suber* in DI; and OA = 63.4 %, κ = 0.44 for *Q. ilex*, and OA = 53.3 %, κ = 0.31 for *Q. suber* in DS.

Further analysis revealed specific accuracy metrics for each DS category pair. The random forest model displayed stronger performance in distinguishing between the early stages of the disease in *Q. ilex*, with an OA of 70.0 % for DS 0–1. However, it was less effective for *Q. suber*, with an OA of 66.2 % for the same DS category. The support vector machine showed a similar pattern, but with a marginally lower accuracy for these early stages. This additional layer of results (Appendix C) underscores the need for improved early detection methods in our disease

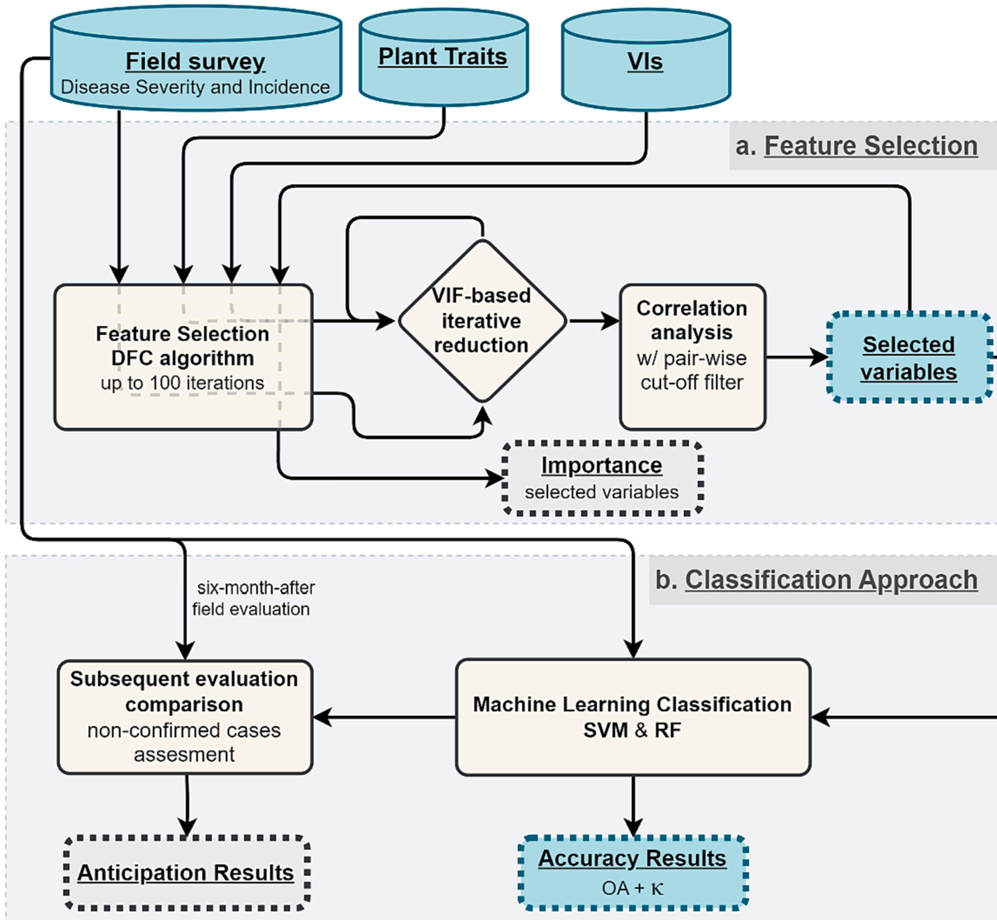


**Fig. 7.** Data analysis workflow: plant functional traits and vegetation indices selection to evaluate the performance of the classification model for the determination of the physiological state of the vegetation. Section a) illustrates the iterative selection of critical variables; section b) outlines the model evaluation using SVM and RF classifiers, with performance validated with field survey data.

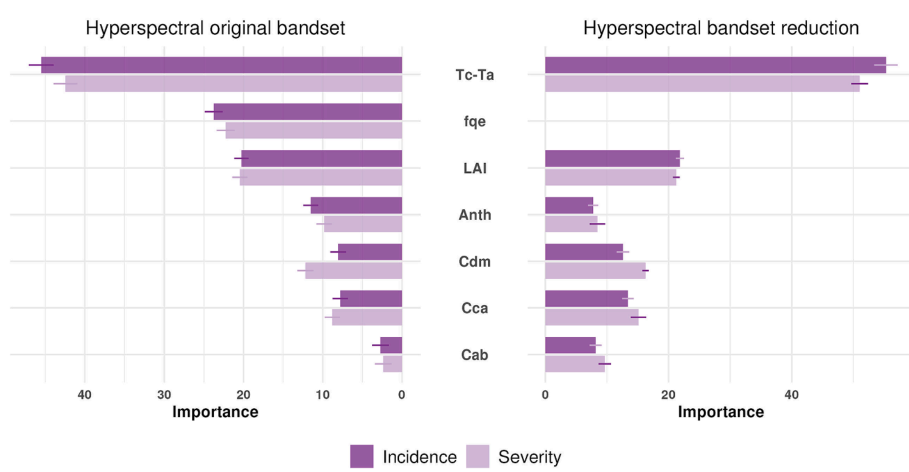


**Fig. 8.** Contribution of the most sensitive plant traits derived from the original hyperspectral data (left) and the bandset reduction product (right). The bars show the mean importance calculated for each variable, and the accompanying horizontal line represents the standard deviation. Note that bandset reduction does not include fluorescence quantum efficiency (fqe) since this feature cannot be derived from this multispectral setup by inversion.

monitoring models.

The findings, when assessing the anticipatory capabilities of the model, indicated a prediction rate of 33 % for cases that were initially classified as asymptomatic but turned out to show any symptoms six months later. Both models showed similar performance under these conditions (RF: 32.2 %; SVM: 33.6 %).

## 4. Discussion

The current study highlights the intricate nature of detecting and analysing oak decline –commonly known as “la seca”– in Mediterranean ecosystems, a phenomenon adversely impacting *Quercus suber* and *Quercus ilex* populations (Rey et al., 2023; Touhami et al., 2020). The

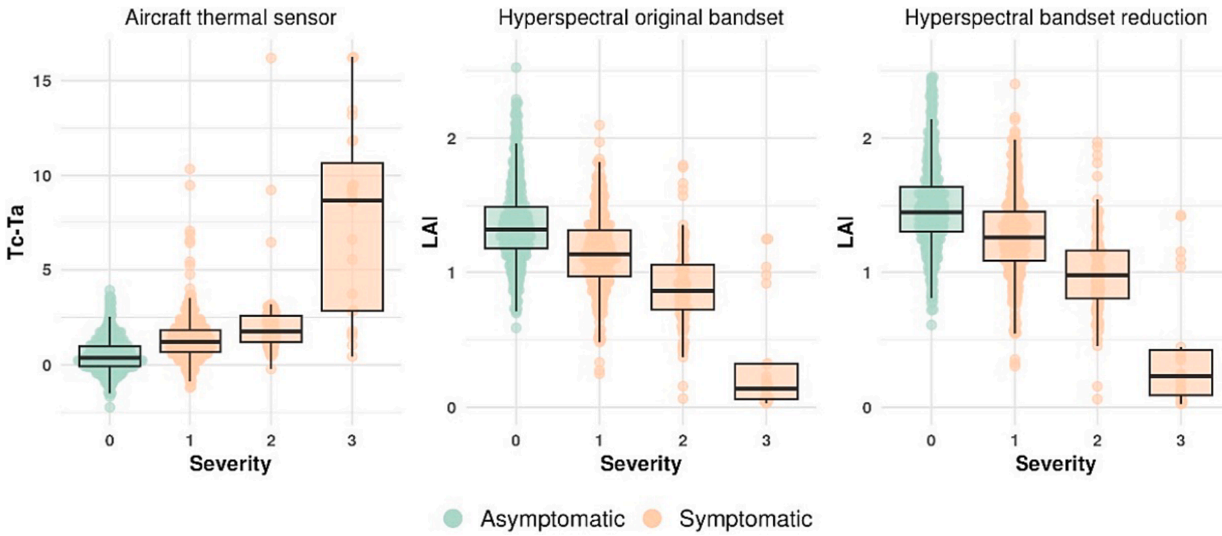


**Fig. 9.** Main plant functional traits (PTs) shared among the different configurations with the original and the bandset reduction. PTs are displayed aggregated over boxplots and dot segregated as jittered points distributed on the x-axis to reduce overplotting.

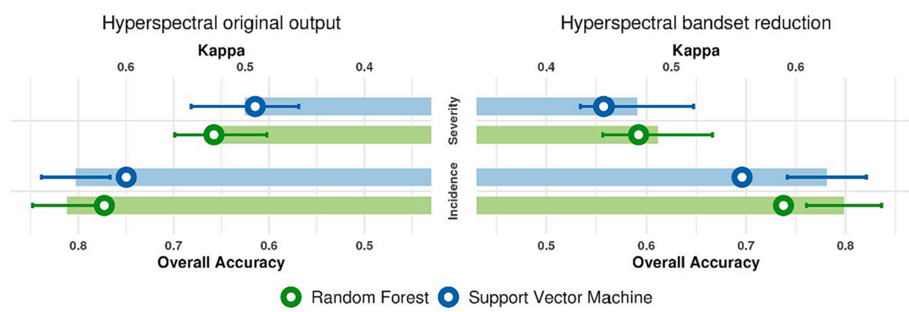


**Fig. 10.** Overall accuracy (OA; horizontal bars), Cohen's kappa coefficient (κ; doughnuts) and respective standard deviations (horizontal lines) of the prediction capability of random forest (RF) and support vector machine models (SVM) for detecting disease incidence (DI) and disease severity (DS) using the full range of bands in the hyperspectral images data (left) and the hyperspectral bandset reduction product (right).

**Table 3**
Predictive performance of random forest and support vector machine models to determine disease incidence and severity using the thermal data, the full range of bands from the hyperspectral imager and the RPAS-based hyperspectral bandset reduction (HBR) dataset. The best and worst values for each case are highlighted in green and red, respectively; darker colours indicate the extremes.

| Dataset | Random Forest | | | | SVM RBF | | | |
|---|---|---|---|---|---|---|---|---|
| | Disease Incidence | | Disease Severity | | Disease Incidence | | Disease Severity | |
| | OA | κ | OA | κ | OA | κ | OA | κ |
| **Thermal** | 0.695 | 0.387 | 0.449 | 0.263 | 0.754 | 0.505 | 0.480 | 0.320 |
| **Hyperspectral** | 0.780 | 0.555 | 0.578 | 0.433 | 0.779 | 0.554 | 0.553 | 0.412 |
| **HBR** | 0.760 | 0.515 | 0.560 | 0.406 | 0.752 | 0.498 | 0.552 | 0.394 |
| **Hypers. + Thermal** | 0.812 | 0.618 | 0.651 | 0.526 | 0.803 | 0.601 | 0.625 | 0.492 |
| **HBR + Thermal** | 0.798 | 0.590 | 0.611 | 0.474 | 0.781 | 0.557 | 0.591 | 0.446 |

urgency of developing advanced analytical methods, as presented in our study, is underscored by the increasing impact of oak decline on the stability and economic viability of dehesa/montado agroforestry systems. These ecosystems, as detailed by Sá-Sousa (2014), are not only rich in biodiversity but also crucial for regional economies, especially in cork production and Iberian pig farming. Our findings address the critical need for timely and accurate detection of forest decline, which is essential for planning and implementing effective restoration and reforestation strategies.

In exploring the potential use of RPAS imagery for precision mapping and spatial management of oak decline, our study extends the work of Hornero et al., (2021b) in utilising airborne hyperspectral sensors for the prediction of decline. We highlight the practical limitations of airborne precision mapping, noted by Alderotti and Verdiani (2023), and propose

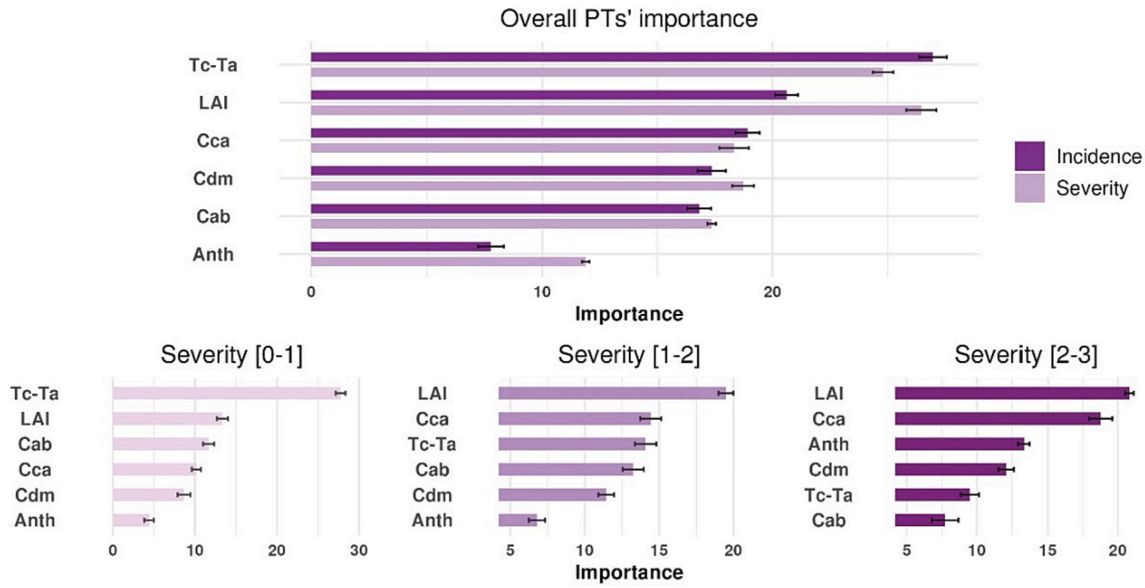


**Fig. 11.** Importance score for plant traits (PTs) computed via DFC algorithm in detecting oak decline is shown at the top. Bottom plots show the importance score while discriminating between severity stages.

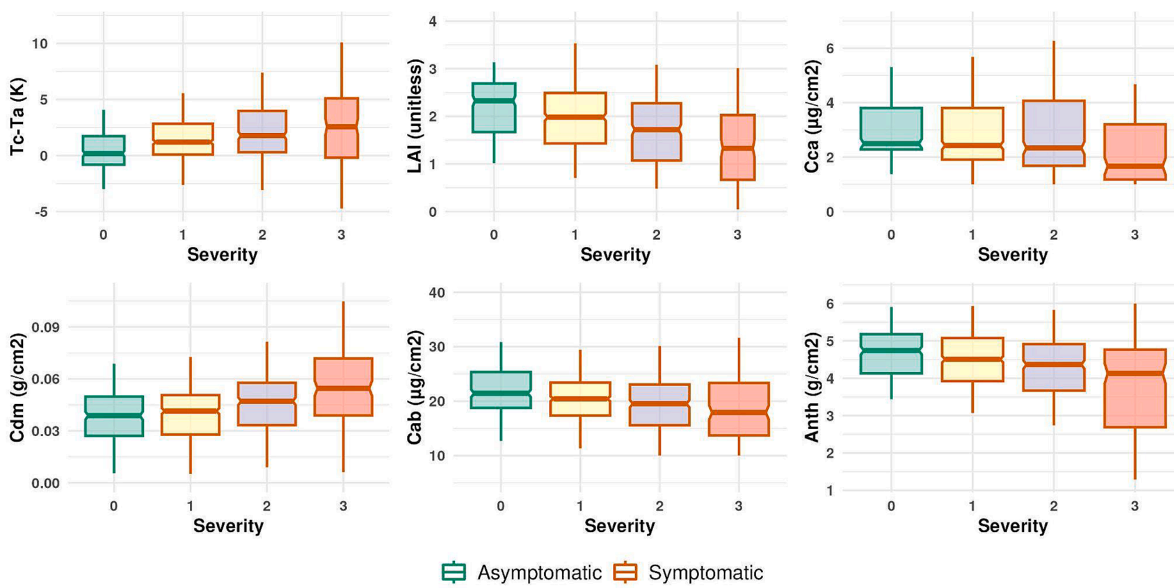


**Fig. 12.** Plant traits displayed aggregated over boxplots and levels of severity of asymptomatic and symptomatic trees.

RPAS imagery as a cost-efficient alternative. Despite the constraints associated with low-cost acquisition systems (Grznárová et al., 2019), our approach demonstrates that band reduction analysis from hyperspectral and thermal imagery is a critical step in developing effective forest health monitoring tools.

The results indicate that using hyperspectral data alone yields better results compared with relying solely on HBR data. This finding reinforces the notion that the comprehensive spectrum captured by hyperspectral imaging provides nuanced information for oak decline detection, as shown by Hernández-Clemente et al. (2017). When flying over large areas, generating hyperspectral and thermal mosaics that are co-aligned can be challenging (Kim et al., 2022). Therefore, it may be more practical to fly only hyperspectral for large areas. However, there are methods available for generating UAV-based hyperspectral mosaics using push-broom sensors, which can help align hyperspectral swaths with RGB photogrammetric orthophoto mosaics (Jurado et al., 2021).

The advantage of using hyperspectral data diminishes when compared to the combined use of HBR and thermal data, where the latter emerges as more effective. This synergy implies that while hyperspectral data is comprehensive, integrating thermal and multispectral data is necessary for robust oak decline detection. It also highlights the critical role of thermal imaging, particularly in enhancing the accuracy of decline detection, possibly due to its ability to capture water stress. These outcomes align with Zarco-Tejada et al.'s (2021) findings, which underscore the contribution of plant traits from hyperspectral and thermal imagery to differentiate between biotic and abiotic stressors in olive trees impacted by *Xylella fastidiosa*. In oak forests affected by decline, symptoms of water stress can closely resemble those caused by *phytophthora* infections, leading to possible misidentification (Martín-Sánchez et al., 2022). Thus, this research underscores the combined use of HBR and thermal data, highlighting their critical role in forest management and ecological research.

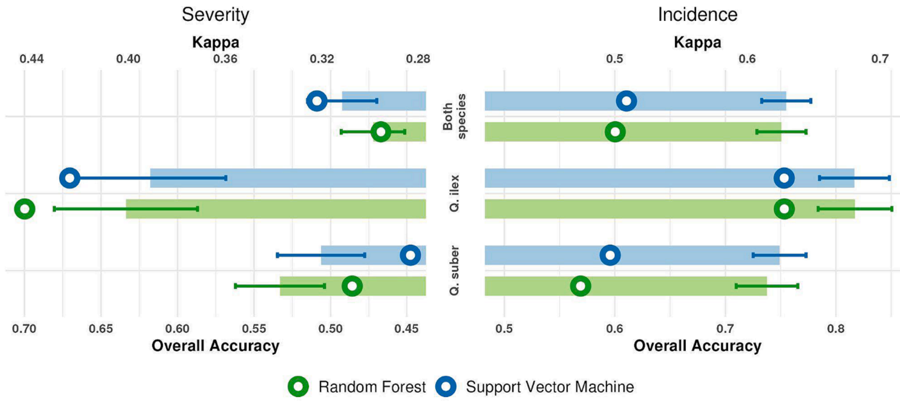


**Fig. 13.** Holm-oak and Cork-oak decline overall accuracies and Cohen's kappa scores for the classification model using RPAS-based models, using all locations for both species (top bars) and then segregated by species underneath.

The retrieval of PTs from radiative transfer models and ML techniques used in this study is essential to understanding forest decline processes and has allowed the cross-comparison of model performance between different band configurations. Previous studies have shown, using airborne image data, the importance of quantifying PTs to understand vegetation responses to pest infestations such as *Xylella fastidiosa* in olive and almond trees (Zarco-Tejada et al., 2021), *Dothistroma* needle blight in radiata pine (Watt et al., 2023), or *Phytophthora Cinamomi* in oak trees (Hornero et al., 2021b). However, the retrieval of PTs is constrained by the available spectral resolution of the sensors, which is generally quite limited in low-cost systems. In this work, we have demonstrated that this limitation is reduced by the high contribution of thermal data as indicators to discriminate DI and DS in oak forests. The results are aligned with previous studies focused on the analysis of RPAS-based lightweight thermal imagery for the quantification of PTs, such as evapotranspiration or stomatal conductance (Hoffmann et al., 2016) or for the detection of water stress in vineyards (Santesteban et al., 2017).

A crucial factor in forest decline management is to be able to quantify both incidence and severity levels. This allows each type of damage and species to be characterised at a specific level of severity and to assess both gradual and total patterns of change. These parameters have been considered fundamental for the global characterisation of forest damage at the European level and are currently included in the harmonised database generated by the European Commission DEFID2 (Forzieri et al., 2023). In the context of disease severity, our research corroborates the negative correlation between increasing Tc-Ta values and LAI, as well as the associated pigment content levels, which is in line with previous research indicating that heightened stress levels result in a reduction of LAI, a key physiological trait (Zarco-Tejada et al., 2021).

The ML models employed in this study have shown a fair to good capability in discriminating between different stages of decline, with *Q. ilex* yielding higher accuracies than *Q. suber*. This differential response highlights species-specific sensitivities to stress factors, which could be attributed to inherent physiological or structural differences between species. Despite the demonstrated utility of RPAS-based imaging in this study, we must acknowledge the existing limitations. For instance, the stability of RPASs and the spectral quality of images can be compromised by vibrations and payload weight restrictions (Honkavaara et al., 2017). Furthermore, the restricted flight endurance of RPAS platforms may pose challenges in conducting comprehensive assessments over large forested areas. These technical challenges necessitate ongoing technological advancements and methodological improvements to fully exploit RPASs' potential for forest health monitoring.

Given the simple nature of the binary grouping compared to the nuanced multilevel categorisation, DI classification yielded significantly better results than DS. This highlights the challenges posed by severity classification; the ML models show better performance in identifying more advanced stages of the disease, while it is more difficult to detect the early stages, which is critical to stop the spread of the disease. The difference in model performance between *Q. ilex* and Q. *suber* also raises questions about the broader applicability of RPAS-based sensors across species. The potential for species-specific calibration of sensors and algorithms should be explored in future research to enhance the sensitivity and accuracy of decline detection methods. In addition, the integration of RPAS-based data with satellite imagery could potentially address the limitations in spatial coverage and temporal frequency, offering a more comprehensive monitoring system.

The findings demonstrate a modest prediction rate of approximately one-third for cases that transitioned from an asymptomatic to a symptomatic state within a six-month period. To overcome the subjective nature of field visual inspection, which is crucial for training and validating our models, future studies could consider using ground-based photogrammetry as complementary to visual interpretation, an approach that could potentially increase the accuracy and objectivity in assessing tree decline. The anticipatory performance of the predictive models still needs to be assessed with longer time series data over a large dataset of true positive and negative values of severity, especially for detecting early damage stages without visual variations in LAI. The similar performance metrics between the random forest and support vector machine models, with RF at 32.2 % and SVM slightly higher at 33.6 %, suggest that both algorithms possess comparable predictive strengths under the conditions tested. While not overwhelmingly high, this accuracy level still represents a significant advancement in our ability to forecast forest decline before the manifestation of visible symptoms. The models' capacity to identify a subset of trees that would develop symptoms suggests a potential for these models to be refined further. Enhancing their predictive accuracy could substantially aid in proactive forest health management, allowing interventions to be more strategically targeted and potentially more effective. The convergence of performance also indicates that similar underlying patterns are being captured by both models, which could provide a basis for future model improvement and optimisation.

This proposed method aligns with the urgent need for rapid forest monitoring and the detection of declining oak trees. While RPAS-based multispectral and thermal imagery presents a viable solution for detecting oak decline, the complexities associated with its implementation must be carefully navigated for monitoring functional changes. Future research should aim to refine RPAS-based detection methods, extend their application across different tree species, improve early detection, and integrate them into a multi-scaled approach for forest health monitoring. To this end, our approach can be adapted for other tree species with similar stress responses and integrated into broader forest management strategies, enhancing early intervention capabilities. The scalability of this methodology for extensive forest health surveillance, coupled with advancements in machine learning and high-resolution remote sensing, will be pivotal in addressing the growing challenges posed by climate change and human activities. As the pressures of climate change and anthropogenic activities intensify, the development of precise, scalable, and cost-effective tools for environmental monitoring will become more critical.

## 5. Conclusions

This research advances precision forestry by demonstrating the effectiveness of miniaturised sensors on RPAS platforms, combined with 3-D RTM and machine learning, in detecting forest decline. Despite spectral limitations, RPAS-based multispectral imagery has proven capable of monitoring critical PTs to differentiate stages of decline. And thermal data, especially the temperature differential between the tree canopy and surrounding air (Tc-Ta), significantly enhances disease indicator identification. Tc-Ta and PTs like LAI, derived from HBR, have notably improved model accuracy for detecting oak decline incidence and severity detection, indicating a modest reduction in OA for DI and a marginally greater reduction for DS compared to the model accuracy achieved using hyperspectral and thermal datasets. While using hyperspectral data alone is slightly less accurate than when combined with thermal data, integrating multispectral with thermal is vital to ensure fair to good kappa for severity and incidence detection. These results underscore the need to use PTs and thermal data to assess physiological changes from oak decline with RPASs.

The study confirms the feasibility of detecting oak decline across different severity levels, incidence, and oak species using accessible technology. It opens avenues for species-specific calibration of RPAS-based sensors, paving the way for more accurate detection techniques. The differential accuracies between *Q. ilex* and *Q. suber* suggest that tailored approaches might be required for different species, a consideration that could have significant implications for forest health interventions. The combined use of RTM and RPAS imagery emerges as a crucial approach in vegetation monitoring, enabling the generation of recurrent PT maps that enrich our understanding of plant physiological conditions and the detection of decline phenomena.

## CRediT authorship contribution statement

**A. Hornero:** Writing – review & editing, Writing – original draft, Visualization, Project administration, Methodology, Investigation, Funding acquisition, Formal analysis, Data curation, Conceptualization. **P.J. Zarco-Tejada:** Resources, Investigation. **I. Marengo:** Resources, Funding acquisition. **N. Faria:** Resources, Project administration. **R. Hernández-Clemente:** Writing – review & editing, Resources, Funding acquisition, Conceptualization.

## Declaration of competing interest

The authors declare that they have no known competing financial interests or personal relationships that could have appeared to influence the work reported in this paper.

## Data availability

Data will be made available on request.

## Acknowledgements

This work was supported by La Caixa Foundation, in partnership with BPI and FCT, in the context of the initiative *Promove2020 – O Futuro do Interior*. Data collection and processing were partially supported by the QUERCUSAT (CGL2013-40790-R), ESPECTRAMED (CGL2018-86161-R) and D-TRAITS (PID2021-124058OA-I00) projects, part of the Spanish Research Agency, Ministry of Science and Innovation. The study area was selected in collaboration with ACPA project partners. A. Molina and N. Vargas are acknowledged for their support during the RPAS campaign.

## Appendix

*Appendix A. Vegetation indices derived from the multispectral imagery bandset*

| Vegetation Index | Equation |
|---|---|
| *Normalised Difference Vegetation Index* | $NDVI = (R_{842} - R_{668})/(R_{842} + R_{668})$ |
| *Near-Infrared Reflectance of Vegetation* | $NIR_V = R_{842}(R_{842} - R_{668})/(R_{842} + R_{668})$ |
| *Renormalised Difference Vegetation Index* | $RDVI = (R_{842} - R_{668})/\sqrt{(R_{842} + R_{668})}$ |
| *Modified Simple Ratio* | $MSR = \dfrac{\frac{R_{842}}{R_{668}} - 1}{\left(\frac{R_{842}}{R_{668}}\right)^{0.5} + 1}$ |
| *Optimized Soil-Adjusted Vegetation Index* | $OSAVI = (1 + 0.16)\dfrac{R_{842} - R_{668}}{R_{842} + R_{668} + 0.16}$ |
| *Modified Triangular Vegetation Index 1* | $MTVI_1 = 1.2(1.2(R_{842} - R_{560}) - 2.5(R_{668} - R_{560}))$ |
| *Modified Chlorophyll Absorption Ratio Index* | $MCARI = ((R_{717} - R_{668}) - 0.2(R_{717} - R_{560}))\left(\frac{R_{717}}{R_{668}}\right)$ |
| *Modified Chlorophyll Absorption Ratio Index 1* | $MCARI_1 = 1.2(2.5(R_{842} - R_{668}) - 1.3(R_{842} - R_{560}))$ |
| *Modified Chlorophyll Absorption Ratio Index 2* | $MCARI_2 = 1.5\dfrac{2.5(R_{842} - R_{560}) - 1.3(R_{668} - R_{560})}{\sqrt{(2R_{842} + 1)^2 - (6R_{842} - 5\sqrt{R_{668}}) - 0.5}}$ |
| *Enhanced Vegetation Index* | $EVI = 2.5(R_{842} - R_{668})/(R_{842} + 6R_{668} - 7.5R_{475} + 1)$ |
| *Gitelson and Merzlyak 1* | $GM_1 = R_{717}/R_{560}$ |
| *Transformed Chlorophyll Absorption Ratio* | $TCARI = 3\left((R_{717} - R_{668}) - 0.2(R_{717} - R_{560})\frac{R_{717}}{R_{668}}\right)$ |
| *TCARI/OSAVI* | $TCARI/OSAVI = \dfrac{TCARI}{OSAVI}$ |
| *Triangular Vegetation Index* | $TVI = 0.5(120(R_{717} - R_{560}) - 200(R_{668} - R_{560}))$ |
| *Simple Ratio Pigment Index* | $SRPI = R_{475}/R_{668}$ |
| *Normalized Pigment Chlorophyll Index* | $NPCI = (R_{668} - R_{475})/(R_{668} + R_{475})$ |
| *Datt Cab Cx + c Index* | $DCabxc = R_{668}/(3R_{560}R_{717})$ |
| *Datt NIR Cab Cx + c Index* | $DNCabxc = R_{842}/(R_{560}R_{717})$ |

(*continued on next page*)

(*continued*)

| Vegetation Index | Equation |
|---|---|
| *Structure Insensitive Pigment Index* | $SIPI = (R_{842} - R_{475})/(R_{842} + R_{668})$ |
| *Chlorophyll Reciprocal Reflectance Index 700* | $CRI_{700} = 1/R_{475} - 1/R_{717}$ |
| *Modified Chlorophyll Reciprocal Reflectance Index 700* | $CRI_{700m} = 1/R_{560} - 1/R_{717}$ |
| *Near-Infrared Chlorophyll Reciprocal Reflectance Index 550* | $RCRI_{550} = 1/R_{475} - (1/R_{560})R_{842}$ |
| *Near-Infrared Chlorophyll Reciprocal Reflectance Index 700* | $RCRI_{700} = 1/R_{475} - (1/R_{717})R_{842}$ |
| *Plant Senescence Reflectance Index* | $PSRI = (R_{668} - R_{475})/R_{717}$ |
| *Lichtenthaler 3* | $LIC_3 = R_{475}/R_{717}$ |
| *Photochemical Reflectance Index* | $PRI = (R_{560} - R_{475})/(R_{560} + R_{475})$ |
| *Normalised PRI* | $PRIn = PRI/(RDVIR_{717}/R_{668})$ |
| *PRI × CI* | $PRI\ddot{a}CI = PRI(R_{842}/R_{717} - 1)$ |
| *Relative Greenness Index* | $RGI = R_{668}/R_{560}$ |
| *Lichtenthaler 2* | $LIC_2 = R_{475}/R_{668}$ |
| *Pigment Specific Simple Ratio A* | $PSSR_a = R_{842}/R_{668}$ |
| *Pigment Specific Simple Ratio C* | $PSSR_c = R_{842}/R_{475}$ |
| *Pigment Specific Normalised Difference C* | $PSND_c = (R_{842} - R_{475})/(R_{842} + R_{475})$ |
| *Visible Atmospherically Resistant Index* | $VARI = (R_{560} - R_{668})/(R_{560} + R_{668} - R_{475})$ |
| *Anthocyanin Reflectance Index* | $ARI = 1/R_{560} - 1/R_{717}$ |
| *Modified Anthocyanin Reflectance Index* | $mARI = R_{842}(1/R_{560} - 1/R_{717})$ |

*Appendix B. Ranges of parameters used to perform simulations with the FLIGHT RTM*

| Variable | Units | Acronym | Phase 1 | Phase 2 |
|---|---|---|---|---|
| Chlorophyll $a + b$ content | $\mu g\ cm^{-2}$ | $C_{ab}$ | 10–60 | 21–33 |
| Carotenoid content | $\mu g\ cm^{-2}$ | $C_{ar}$ | 1–20 | 1–7 |
| Water content | Cm | $C_w$ | 0.013 | 0–0.03 |
| Dry matter content | $g\ cm^{-2}$ | $C_{dm}$ | 0.024 | 0.003–0.018 |
| Anthocyanin content | $g\ cm^{-2}$ | $A_{nth}$ | 0 | 0–6 |
| Senescence material | Fraction | $C_s$ | 0 | 0 |
| Mesophyll structure | – | N | 2.1 | 2.1 |
| Leaf area index | $m^2\ m^{-2}$ | LAI | 0–4 | 0.1–2.5 |
| Leaf size | m | LFS | 0.05 | 0.05 |
| Leaf angle distribution | – | LAD | Spherical | Spherical |
| Soil reflectance | % | Soil | 3 samples | 3 samples |
| Crowns shape | – | CSh | Ellipsoid | Ellipsoid |
| Solar Zenith | deg. | SZA | 36.67 | 36.67 |
| Solar Azimuth | deg. | SAA | 115.76 | 115.76 |

*Appendix C. Predictive performance of random forest and support vector machine models for determining disease incidence (DI), disease severity (SD) and clustering of severity classes with each adjacent level (severities 0–1; severities 1–2; and severities 2–3), using multispectral and thermal RPAS on-board sensor data. The best and worst values are highlighted in green and red, respectively. No symbol is shown for accuracy P values above 0.05; * P ≤ 0.05; and ** P ≤ 0.01. Darker shades indicate the extremes, while lighter ones denote a secondary rank in each case.*

| Dataset | Model | DI | | DS | | DS 0–1 | | DS 1–2 | | DS 2–3 | |
|---|---|---|---|---|---|---|---|---|---|---|---|
| | | OA | κ | OA | κ | OA | κ | OA | κ | OA | κ |
| **Both species** | Random Forest | 0.751** | 0.504 | 0.472** | 0.296 | 0.668* | 0.336 | 0.636 | 0.270 | 0.655 | 0.305 |
| ***Q. Ilex*** | | 0.817* | 0.627 | 0.634 | 0.443 | 0.700 | 0.395 | 0.687 | 0.371 | 0.731 | 0.449 |
| ***Q. Suber*** | | 0.738* | 0.474 | 0.533 | 0.308 | 0.662 | 0.324 | 0.655 | 0.309 | 0.628 | 0.255 |
| **Both species** | SVM RBF | 0.755** | 0.509 | 0.492** | 0.322 | 0.664* | 0.326 | 0.643 | 0.285 | 0.659 | 0.314 |
| ***Q. Ilex*** | | 0.818* | 0.628 | 0.618 | 0.424 | 0.684 | 0.362 | 0.708 | 0.410 | 0.717 | 0.426 |
| ***Q. Suber*** | | 0.749** | 0.496 | 0.506 | 0.283 | 0.642 | 0.284 | 0.654 | 0.306 | 0.636 | 0.272 |

## References


Alderotti, F., Verdiani, E., 2023. God save the queen! How and why the dominant evergreen species of the Mediterranean Basin is declining? AoB PLANTS 15, plad051. https://doi.org/10.1093/aobpla/plad051.

Breiman, L., 2001. Random Forests. Mach. Learn. 45, 5–32. https://doi.org/10.1023/A:1010933404324.

Calderón, R., Navas-Cortés, J.A., Zarco-Tejada, P.J., 2015. Early Detection and Quantification of Verticillium Wilt in Olive Using Hyperspectral and Thermal Imagery over Large Areas. Remote Sens. (Basel) 7, 5584–5610. https://doi.org/10.3390/rs70505584.

Camilo-Alves, C.S.P., Vaz, M., Da Clara, M.I.E., Ribeiro, N.M.D.A., 2017. Chronic cork oak decline and water status: new insights. New For. 48, 753–772. https://doi.org/10.1007/s11056-017-9595-3.

Castellaneta, M., Rita, A., Camarero, J.J., Colangelo, M., Ripullone, F., 2022. Declines in canopy greenness and tree growth are caused by combined climate extremes during drought-induced dieback. Sci. Total Environ. 813, 152666 https://doi.org/10.1016/j.scitotenv.2021.152666.

Colangelo, M., Camarero, J.J., Borghetti, M., Gentilesca, T., Oliva, J., Redondo, M.-A., Ripullone, F., 2018. Drought and Phytophthora Are Associated With the Decline of Oak Species in Southern Italy. Front. Plant Sci. 9 https://doi.org/10.3389/fpls.2018.01595.

Consejería de Medio Ambiente y Ordenación del Territorio, 2018. Manual para el establecimiento y la evaluación de las parcelas de la Red Andaluza de Seguimiento de Daños sobre Ecosistemas Forestales: Red SEDA y Red de PINSAPO. Junta de Andalucía.

Contreras-Cornejo, H.A., Larsen, J., Fernández-Pavía, S.P., Oyama, K., 2023. Climate change, a booster of disease outbreaks by the plant pathogen Phytophthora in oak forests. Rhizosphere 27, 100719. https://doi.org/10.1016/j.rhisph.2023.100719.

Camilo-Alves, C. de S. e P., Clara, M.I.E. da, Ribeiro, N.M.C. de A., 2013. Decline of Mediterranean oak trees and its association with Phytophthora cinnamomi: a review. Eur J Forest Res 132, 411–432. https://doi.org/10.1007/s10342-013-0688-z.

Dormann, C.F., Elith, J., Bacher, S., Buchmann, C., Carl, G., Carré, G., Marquéz, J.R.G., Gruber, B., Lafourcade, B., Leitão, P.J., Münkemüller, T., McClean, C., Osborne, P.E., Reineking, B., Schröder, B., Skidmore, A.K., Zurell, D., Lautenbach, S., 2013. Collinearity: a review of methods to deal with it and a simulation study evaluating their performance. Ecography 36, 27–46. https://doi.org/10.1111/j.1600-0587.2012.07348.x.

Ecke, S., Dempewolf, J., Frey, J., Schwaller, A., Endres, E., Klemmt, H.-J., Tiede, D., Seifert, T., 2022. UAV-Based Forest Health Monitoring: A Systematic Review. Remote Sens. (Basel) 14, 3205. https://doi.org/10.3390/rs14133205.

Eichhorn, J., Roskams, P., Ferretti, M., Mues, V., Szepesi, A., 2016. Visual assessment of crown condition and damaging agents. Manual Part IV, in: Manual on methods and criteria for harmonized sampling, assessment, monitoring and analysis of the effects of air pollution on forests. UNECE ICP Forests Programme Co-ordinating Centre, Eberswalde, Germany, p. 49.

Feret, J.-B., Gitelson, A., Noble, S.D., Jacquemoud, S., 2017. PROSPECT-D: Towards modeling leaf optical properties through a complete lifecycle. Remote Sens. Environ. 193, 204–215. https://doi.org/10.1016/j.rse.2017.03.004.

Fleiss, J.L., Levin, B., Paik, M.C., Fleiss, J., 2003. Statistical Methods for Rates & Proportions. Hoboken, N.J.

Forzieri, G., Dutrieux, L.P., Elia, A., Eckhardt, B., Caudullo, G., Taboada, F.Á., Andriolo, A., Bălăcenoiu, F., Bastos, A., Buzatu, A., Dorado, F.C., Dobrovolný, L., Duduman, M.-L., Fernandez-Carrillo, A., Hernández-Clemente, R., Hornero, A., Ionuț, S., Lombardero, M.J., Junttila, S., Lukeš, P., Marianelli, L., Mas, H., Mlčoušek, M., Mugnai, F., Nețoiu, C., Nikolov, C., Olenici, N., Olsson, P.-O., Paoli, F., Paraschiv, M., Patočka, Z., Pérez-Laorga, E., Quero, J.L., Rüetschi, M., Stroheker, S., Nardi, D., Ferenčík, J., Battisti, A., Hartmann, H., Nistor, C., Cescatti, A., Beck, P.S. A., 2023. The Database of European Forest Insect and Disease Disturbances: DEFID2. Glob. Chang. Biol. https://doi.org/10.1111/gcb.16912.

Fraser, B.T., Congalton, R.G., 2021. Monitoring Fine-Scale Forest Health Using Unmanned Aerial Systems (UAS) Multispectral Models. Remote Sens. (Basel) 13, 4873. https://doi.org/10.3390/rs13234873.

Gigović, L., Pourghasemi, H.R., Drobnjak, S., Bai, S., 2019. Testing a New Ensemble Model Based on SVM and Random Forest in Forest Fire Susceptibility Assessment and Its Mapping in Serbia's Tara National Park. Forests 10, 408. https://doi.org/10.3390/f10050408.

Gznárová, A., Mokroš, M., Surový, P., Slavík, M., Pondelík, M., Merganič, J., 2019. THE CROWN DIAMETER ESTIMATION FROM FIXED WING TYPE OF UAV IMAGERY. The International Archives of the Photogrammetry, Remote Sensing and Spatial Information Sciences XLII-2-W13, 337–341. https://doi.org/10.5194/isprs-archives-XLII-2-W13-337-2019.

He, J., Cheng, M.X., 2021. Weighting Methods for Rare Event Identification From Imbalanced Datasets. Front Big Data 4, 715320. https://doi.org/10.3389/fdata.2021.715320.

Hernández-Clemente, R., Navarro-Cerrillo, R.M., Zarco-Tejada, P.J., 2012. Carotenoid content estimation in a heterogeneous conifer forest using narrow-band indices and PROSPECT+DART simulations. Remote Sens. Environ. 127, 298–315. https://doi.org/10.1016/j.rse.2012.09.014.

Hernández-Clemente, R., North, P.R.J., Hornero, A., Zarco-Tejada, P.J., 2017. Assessing the effects of forest health on sun-induced chlorophyll fluorescence using the FluorFLIGHT 3-D radiative transfer model to account for forest structure. Remote Sens. Environ. 193, 165–179. https://doi.org/10.1016/j.rse.2017.02.012.

Hernández-Clemente, R., Hornero, A., Mottus, M., Penuelas, J., González-Dugo, V., Jiménez, J.C., Suárez, L., Alonso, L., Zarco-Tejada, P.J., 2019. Early Diagnosis of Vegetation Health From High-Resolution Hyperspectral and Thermal Imagery: Lessons Learned From Empirical Relationships and Radiative Transfer Modelling. Curr Forestry Rep 5, 169–183. https://doi.org/10.1007/s40725-019-00096-1.

Hernández-Lambraño, R.E., de la Cruz, D.R., Sánchez-Agudo, J.Á., 2019. Spatial oak decline models to inform conservation planning in the Central-Western Iberian Peninsula. For. Ecol. Manage. 441, 115–126. https://doi.org/10.1016/j.foreco.2019.03.028.

Hoffmann, H., Jensen, R., Thomsen, A., Nieto, H., Rasmussen, J., Friborg, T., 2016. Crop water stress maps for an entire growing season from visible and thermal UAV imagery. Biogeosciences 13, 6545–6563. https://doi.org/10.5194/bg-13-6545-2016.

Honkavaara, E., Rosnell, T., Oliveira, R., Tommaselli, A., 2017. Band registration of tuneable frame format hyperspectral UAV imagers in complex scenes. ISPRS Journal of Photogrammetry and Remote Sensing 134, 96–109. https://doi.org/10.1016/j.isprsjprs.2017.10.014.

Hornero, A., North, P.R.J., Zarco-Tejada, P.J., Rascher, U., Martín, M.P., Migliavacca, M., Hernandez-Clemente, R., 2021a. Assessing the contribution of understory sun-induced chlorophyll fluorescence through 3-D radiative transfer modelling and field data. Remote Sens. Environ. 253, 112195 https://doi.org/10.1016/j.rse.2020.112195.

Hornero, A., Zarco-Tejada, P.J., Quero, J.L., North, P.R.J., Ruiz-Gómez, F.J., Sánchez-Cuesta, R., Hernandez-Clemente, R., 2021b. Modelling hyperspectral- and thermal-based plant traits for the early detection of Phytophthora-induced symptoms in oak decline. Remote Sens. Environ. 263, 112570 https://doi.org/10.1016/j.rse.2021.112570.

Jung, T., Blaschke, H., Oßwald, W., 2000. Involvement of soilborne Phytophthora species in Central European oak decline and the effect of site factors on the disease. Plant Pathol. 49, 706–718. https://doi.org/10.1046/j.1365-3059.2000.00521.x.

Jurado, J.M., Pádua, L., Hruška, J., Feito, F.R., Sousa, J.J., 2021. An Efficient Method for Generating UAV-Based Hyperspectral Mosaics Using Push-Broom Sensors. IEEE J. Sel. Top. Appl. Earth Obs. Remote Sens. 14, 6515–6531. https://doi.org/10.1109/JSTARS.2021.3088945.

Kim, J.-I., Chi, J., Masjedi, A., Flatt, J.E., Crawford, M.M., Habib, A.F., Lee, J., Kim, H.-C., 2022. High-resolution hyperspectral imagery from pushbroom scanners on unmanned aerial systems. Geosci. Data J. 9, 221–234. https://doi.org/10.1002/gdj3.133.

Kursa, M.B., Rudnicki, W.R., 2010. Feature Selection with the Boruta Package. J. Stat. Softw. 36, 1–13. https://doi.org/10.18637/jss.v036.i11.

Landis, J.R., Koch, G.G., 1977. The Measurement of Observer Agreement for Categorical Data. Biometrics 33, 159–174. https://doi.org/10.2307/2529310.

Liu, P., Choo, K.-K.-R., Wang, L., Huang, F., 2017. SVM or deep learning? A comparative study on remote sensing image classification. Soft Comput 21, 7053–7065. https://doi.org/10.1007/s00500-016-2247-2.

Liu, D., Kelly, M., Gong, P., Guo, Q., 2007. Characterizing spatial–temporal tree mortality patterns associated with a new forest disease. For. Ecol. Manage. 253, 220–231. https://doi.org/10.1016/j.foreco.2007.07.020.

Maes, W.H., Huete, A.R., Steppe, K., 2017. Optimizing the Processing of UAV-Based Thermal Imagery. Remote Sens. (Basel) 9, 476. https://doi.org/10.3390/rs9050476.

Martín-Sánchez, R., Peguero-Pina, J.J., Alonso-Forn, D., Ferrio, J.P., Sancho-Knapik, D., Gil-Pelegrín, E., 2022. Summer and winter can equally stress holm oak (Quercus ilex L.) in Mediterranean areas: A physiological view. Flora 290, 152058. https://doi.org/10.1016/j.flora.2022.152058.

North, P.R.J., 1996. Three-dimensional forest light interaction model using a Monte Carlo method. IEEE Trans. Geosci. Remote Sens. 34, 946–956. https://doi.org/10.1109/36.508411.

Olbrycht, R., Więcek, B., 2015. New approach to thermal drift correction in microbolometer thermal cameras. Quantitative InfraRed Thermography Journal 12, 184–195. https://doi.org/10.1080/17686733.2015.1055675.

Oliveira, R.A., Tommaselli, A.M.G., Honkavaara, E., 2019. Generating a hyperspectral digital surface model using a hyperspectral 2D frame camera. ISPRS J. Photogramm. Remote Sens. 147, 345–360. https://doi.org/10.1016/j.isprsjprs.2018.11.025.

Pause, M., Schweitzer, C., Rosenthal, M., Keuck, V., Bumberger, J., Dietrich, P., Heurich, M., Jung, A., Lausch, A., 2016. In Situ/Remote Sensing Integration to Assess Forest Health—A Review. Remote Sens. (Basel) 8, 471. https://doi.org/10.3390/rs8060471.

Poblete, T., Navas-Cortes, J.A., Hornero, A., Camino, C., Calderon, R., Hernandez-Clemente, R., Landa, B.B., Zarco-Tejada, P.J., 2023. Detection of symptoms induced by vascular plant pathogens in tree crops using high-resolution satellite data: Modelling and assessment with airborne hyperspectral imagery. Remote Sens. Environ. 295, 113698 https://doi.org/10.1016/j.rse.2023.113698.

Rey, M.-D., Labella-Ortega, M., Guerrero-Sánchez, V.M., Carleial, R., Castillejo, M.Á., Ruggieri, V., Jorrín-Novo, J.V., 2023. A first draft genome of holm oak (Quercus ilex subsp. Ballota), the Most Representative Species of the Mediterranean Forest and the Spanish Agrosylvopastoral Ecosystem "dehesa". Frontiers in Molecular Biosciences 10.

Richards, J.A., Jia, X., 1999. Remote Sensing Digital Image Analysis: An Introduction, 3rd ed. Springer-Verlag, Berlin Heidelberg. https://doi.org/10.1007/978-3-662-03978-6.

Santesteban, L.G., Di Gennaro, S.F., Herrero-Langreo, A., Miranda, C., Royo, J.B., Matese, A., 2017. High-resolution UAV-based thermal imaging to estimate the instantaneous and seasonal variability of plant water status within a vineyard. Agricultural Water Management, Special Issue: Advances on ICTs for Water Management in Agriculture 183, 49–59. https://doi.org/10.1016/j.agwat.2016.08.026.

Sá-Sousa, P., 2014. The Portuguese montado: conciliating ecological values with human demands within a dynamic agroforestry system. Ann. For. Sci. 71, 1–3. https://doi.org/10.1007/s13595-013-0338-0.

Scholkopf, B., Sung, K.-K., Burges, C.J.C., Girosi, F., Niyogi, P., Poggio, T., Vapnik, V., 1997. Comparing support vector machines with Gaussian kernels to radial basis function classifiers. IEEE Trans. Signal Process. 45, 2758–2765. https://doi.org/10.1109/78.650102.

Seem, R.C., 1984. Disease Incidence and Severity Relationships. Annu. Rev. Phytopathol. 22, 133–150. https://doi.org/10.1146/annurev.py.22.090184.001025.

Tian, J., Wang, L., Li, X., Gong, H., Shi, C., Zhong, R., Liu, X., 2017. Comparison of UAV and WorldView-2 imagery for mapping leaf area index of mangrove forest. International Journal of Applied Earth Observation and Geoinformation 61, 22–31. https://doi.org/10.1016/j.jag.2017.05.002.

Touhami, I., Chirino, E., Aouinti, H., El Khorchani, A., Elaieb, M.T., Khaldi, A., Nasr, Z., 2020. Decline and dieback of cork oak (Quercus suber L.) forests in the Mediterranean basin: a case study of Kroumirie. Northwest Tunisia. J. for. Res. 31, 1461–1477. https://doi.org/10.1007/s11676-019-00974-1.

Varner, J.M., Hood, S.M., Aubrey, Doug.P., Yedinak, K., Hiers, J.K., Jolly, W.M., Shearman, T.M., McDaniel, J.K., O'Brien, J.J., Rowell, E.M., 2021. Tree crown injury from wildland fires: causes, measurement and ecological and physiological consequences. New Phytologist. 231, 1676–1685. https://doi.org/10.1111/nph.17539.

Watt, M.S., Poblete, T., de Silva, D., Estarija, H.J.C., Hartley, R.J.L., Leonardo, E.M.C., Massam, P., Buddenbaum, H., Zarco-Tejada, P.J., 2023. Prediction of the severity of Dothistroma needle blight in radiata pine using plant based traits and narrow band indices derived from UAV hyperspectral imagery. Agric. Forest Meteorol. 330, 109294 https://doi.org/10.1016/j.agrformet.2022.109294.

Zarco-Tejada, P.J., Guillén-Climent, M.L., Hernández-Clemente, R., Catalina, A., González, M.R., Martín, P., 2013. Estimating leaf carotenoid content in vineyards using high resolution hyperspectral imagery acquired from an unmanned aerial vehicle (UAV). Agric. For. Meteorol. 171–172, 281–294. https://doi.org/10.1016/j.agrformet.2012.12.013.

Zarco-Tejada, P.J., Camino, C., Beck, P.S.A., Calderon, R., Hornero, A., Hernández-Clemente, R., Kattenborn, T., Montes-Borrego, M., Susca, L., Morelli, M., Gonzalez-Dugo, V., North, P.R.J., Landa, B.B., Boscia, D., Saponari, M., Navas-Cortes, J.A., 2018. Previsual symptoms of Xylella fastidiosa infection revealed in spectral plant-trait alterations. Nat. Plants. https://doi.org/10.1038/s41477-018-0189-7.

Zarco-Tejada, P.J., Poblete, T., Camino, C., Gonzalez-Dugo, V., Calderon, R., Hornero, A., Hernandez-Clemente, R., Román-Écija, M., Velasco-Amo, M.P., Landa, B.B., Beck, P.S.A., Saponari, M., Boscia, D., Navas-Cortes, J.A., 2021. Divergent abiotic spectral pathways unravel pathogen stress signals across species. Nat. Commun. 12, 6088. https://doi.org/10.1038/s41467-021-26335-3.